Advanced Functional Materials

ADVANCED FUNCTIONAL MATERIALS
www.afm-journal.de

RESEARCH ARTICLE OPEN ACCESS

Intrabandgap States Engineering in Functionalized Nanodiamond to Generate Solvated Electrons for Photocatalysis Under Solar Illumination

Benjamin Kiendl[1] | Arsène Chemin[2,3] | Adam H. Day[1,4] | Rocio B. Rodriguez[4] | Sneha Choudhury[2] | Franziska Buchner[1,2] | Kaan Atak[2] | Christoph Merschjann[2] | Emina Hadzifejzovic[5] | Tim D. W. Claridge[5] | Karin Larsson[6] | Amélie Venerosy[7] | Mailis M. Lounasvuori[5] | Natalia Zabarska[8] | Boyan Iliev[8] | Thomas J. S. Schubert[8] | Hugues A. Girard[7,9] | Jean-Charles Arnault[7,9] | John S. Foord[5] | Tristan Petit[2] | Anke Krueger[1,4,10]

[1]Institute for Organic Chemistry, Julius-Maximilians University Würzburg, Würzburg, Germany | [2]Helmholtz-Zentrum Berlin für Materialien und Energie GmbH, Berlin, Germany | [3]Université Claude Bernard Lyon1, UMR5306, CNRS, Institut Lumière Matière, Villeurbanne, France | [4]Institute of Organic Chemistry, University of Stuttgart, Stuttgart, Germany | [5]Chemistry Research Laboratory, University of Oxford, Oxford, UK | [6]Ångström Laboratory for Inorganic Chemistry, Uppsala University, Uppsala, Sweden | [7]CEA, LIST, Diamond Sensors Laboratory, Cedex, Gif sur Yvette, France | [8]IOLITEC Ionic Liquids Technologies GmbH, Heilbronn, Germany | [9]Université Paris-Saclay, CEA, CNRS, NIMBE, CEDEX, Gif-Sur-Yvette, France | [10]Center For Integrated Quantum Science and Technology (IQST), Stuttgart, Germany

Correspondence: Tristan Petit (tristan.petit@helmholtz-berlin.de) | Anke Krueger (anke.krueger@oc.uni-stuttgart.de)

Received: 4 September 2025 | **Revised:** 15 December 2025 | **Accepted:** 29 January 2026

Keywords: bandgap engineering | carbon nanomaterials | photocatalysis | surface chemistry | x-ray spectroscopy

ABSTRACT

Diamond, a wide-bandgap material with unique electronic properties, has shown great promise as a photoreduction catalyst due to its ability to produce highly reductive solvated electrons. However, this requires deep UV illumination, which hampers its sustainable application for real-world photocatalytic processes. Here, it is reported that the tailored introduction of suitable intra-bandgap states in diamond can be achieved by functionalizing nanoscale detonation diamond with a ruthenium-based photosensitizer. The nature of the electronic interaction between the diamond, its surface and the surface-bound moieties is elucidated through X-ray absorption, transient optical absorption, and ultraviolet photoemission spectroscopies both in vacuum and water. The electron emission upon irradiation with visible light is enabled by the surface-induced bangdap engineering. Solar-light-driven reduction of CO_2 to formate is performed as a proof-of-concept reaction. The potential for photoexcited electron transfer (PET) mediated photosensitization in reductive diamond catalysis opens the way for the application of surface-engineered diamond as a sustainable photo(electro)catalyst.

1 | Introduction

The catalyzed reduction of CO_2 into C_1 and value-added hydrocarbon products is a particularly attractive prospect; using a notorious greenhouse gas to produce essential chemical building blocks and therefore has a prominent position in the development of a carbon-neutral industry. Electrochemical reduction of CO_2 can yield a variety of products from predominantly two-, four-, six- and eight- electron reactions to yield formate/formic acid [1–4], CO [5–7], methane [8–10], methanol [11,12], ethanol

---

Benjamin Kiendl, Arsène Chemin, and Adam H. Day contributed equally to this work.

[12], and acetic acid [13]. An effective catalytic system is essential in the reduction of CO_2 due to the significant kinetic barrier associated with disrupting its linear geometry and high bond enthalpy [14]. Because of this, the initial single electron reduction of CO_2 to $CO_2^{\bullet-}$ occurs at a significantly negative potential ($E° = -1.90$ V vs. NHE) [10,15]. In the context of the overall multielectron, multistep reductions, a substantial potential input is required to effect reasonable turnover rates in CO_2 electroreduction [16].

Electro- and photocatalytic CO_2 reduction is widely examined in the literature. Electrocatalytic CO_2 reduction is reasonably efficient with regard to faradaic efficiency (>80% achieved) [1,17,18,19]. However, there remain limitations in product selectivity and realized turnover [9]. Its place within a "green" workflow is particularly hampered by a large energy demand in the form of electricity due to high overpotentials required. In contrast, the potentially very sustainable photocatalytic CO_2 reduction, lacks efficiency due to rapid in-volume electron/hole recombination, achieving a poor yield per quanta of light [10,20]. Thus, novel materials that are able to overcome these hurdles represent an important element in the further development of sustainable CO_2 utilization [21–23].

Boron doped diamond (BDD) is a wide bandgap semiconductor (∼5.5 eV), exhibiting high electrical conductivity and unique surface-termination dependent spectroelectronic properties [24–29]. In addition, it can be produced from biogenic carbon using renewable energy, avoiding the ecological concerns associated with TiO_2 (e.g., nanoparticle toxicity and energy-intensive production) and Cu-based systems (e.g., copper leaching and aquatic toxicity). Additionally, nanodiamonds benefit from existing large-scale industrial production and CVD growth costs are steadily decreasing [29,30]. As a result, BDD presents as an ideal, sustainable material for challenging reduction reactions, with electrocatalytic studies demonstrating high, tunable selectivity to individual products, high faradaic efficiencies, high realized production rates (150 μmol h^{-1} cm^{-2} at −2.5 V vs Ag/AgCl) and excellent stability [2,3,5,31–39]. While demonstrably an excellent electrocatalytic material, the opto-electronic properties of BDD are even more striking. Depending on surface termination (typically with hydrogen) the conduction band of diamond lies above the vacuum level, and the barrier for emission of photoexcited electrons in aqueous media is close to zero, associated with a negative electron affinity (NEA) [20,22,28,40,41]. The ejection of photoexcited electrons in such a manner results in the formation of solvated electrons with significantly negative reduction potentials (−2.9 V vs NHE) [42] and large mean free paths (∼1 µm) and lifetimes (250–300 ns) [43]. Solvated electrons are capable of directly effecting the initial 1-electron reduction of CO_2 without the need for direct substrate-catalyst binding, greatly increasing the available reaction cross-section, resulting in the photoelectrocatalysed reduction of CO_2 with very promising initial results [6].

However, the large BDD bandgap limits its application in sustainable photoelectrocatalysis due to the requirement of high-energy UV (<225 nm) light. Not only does this involve an increased energy requirement for the process, far-UV illumination also results in the degradation of the diamond-aqueous solution interface through surface oxidation (occurring following 2 h illumination), impacting the solvated electron generation and even etching surface carbon from diamond particles [44,45].

Thus, only sub-bandgap photoexcitation of diamond would enable long-lived photocatalytic applications in a sustainable manner. Although a diminished solvated electron generation is observed upon sub-bandgap photoexcitation of unmodified nanodiamond due to the presence of surface defect levels [6,44,47], sufficient numbers of defect-related photoelectrons could only be achieved at the price of a heavily distorted diamond structure eventually compromising the surface-dependent NEA [46,48].

In principle, heteroatom doping using nitrogen or phosphorous as deep donor dopants could provide the required modification of the band structure, however, this approach is limited by the low n-doping efficiency in diamond [49–52]. Alternatively, the introduction of exogenous surface states originating from attached species (photosensitization) is particularly appealing as it does not impact the core-diamond structure, thus avoiding any accompanying changes in photostability, conductivity or mechanical integrity. Functionalization of diamond materials with pyrene and N_3 dye (a ruthenium isothiocyanate bipyridine derivative) exhibited photosensitization of the diamond through hole-donation from the attached sensitizer to the diamond band-structure [53,54]. While of particular interest in substrate oxidation, this route of photosensitization is not suitable for reductive photoelectrocatalysis, and photosensitization through this route is yet to be demonstrated.

Herein, we investigate the engineering of suitable electronic states within the diamond bandgap by functionalization with a ruthenium-trisbipyridine derivative as a novel concept in the development of diamond-based sources of highly reductive photogenerated electrons. $Ru(bpy)_3$ has been shown to be itself not able to catalyze demanding reduction reactions such as CO_2 reduction and has been instead used as a photosensitizer for other, catalytically active compounds [55,56]. The additional electronic levels promote photo-induced electron transfer at the surface of detonation nanodiamond (DND), enabling reductive photo(electro)catalysis using visible light. Furthermore, in decorating a BDD electrode with these nanodiamond particles, the first proof-of-concept of a solar-driven, photoelectrocatalytic CO_2 reduction on diamond is presented.

2 | Results and Discussion

Detonation nanodiamond fully deagglomerated using attrition milling [57] was functionalized with a ruthenium tris-bipyridine derivative complex (**Ru1**) via non-conjugated (**L1**) and conjugated (**L2**) linker systems (Figure 1). The ruthenium trisbipyridine derivative was chosen because of its established optical and electronic properties, its stability and its wide application as a photosensitizer [55,56,58,59]. It was predicted that the frontier molecular orbitals would fit well in the bandgap of diamond, based on comparison with literature [54], and would allow for electronic interaction with the surface of diamond [60]. The precursor complex (**Ru1-C≡CH**) was synthesized according to literature [61] (for details see Supporting Information, Chapter S2.1), exhibiting the required terminal alkyne component for

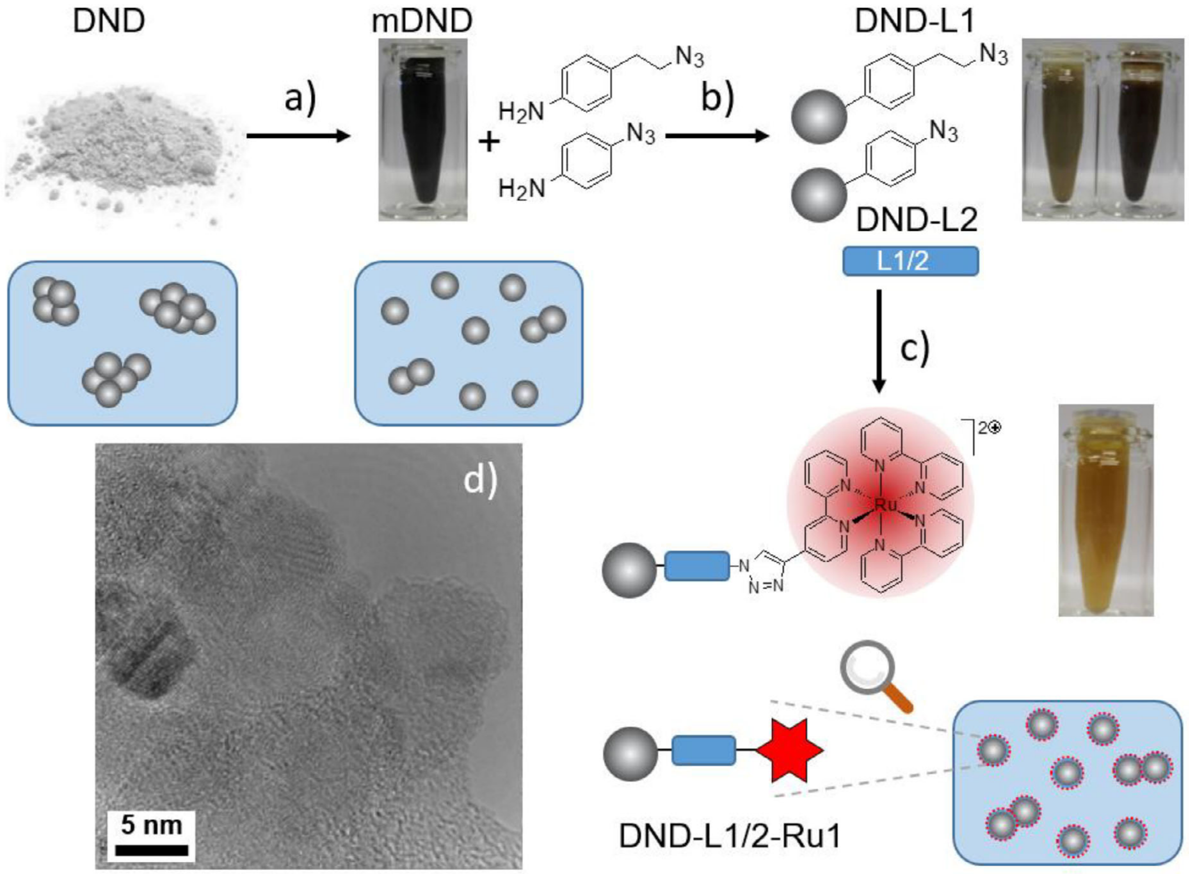

FIGURE 1 | Synthesis and structure of surface functionalized nanodiamond carrying ruthenium complexes as surface bound sensitizers. (a) attrition milling of detonation nanodiamond in water leads to fully dispersed diamond nanoparticles; (b) Diazonium coupling using amyl nitrite in water yields the linker functionalized nanodiamond materials DND-L1 and DND-L2; (c) CuAAC chemistry using Ru1-C≡CH, Ph_3PCuI, sodium ascorbate in DMF/H_2O; (d) TEM image of **DND-L2-Ru1**, scale bar 5 nm.

Cu-azide-alkyne 'click' (CuAAC) ligation to the complementary azide functionalized diamond nanoparticles.

2.1 | Surface Functionalized Nanodiamond

Azide functionalized DND particle dispersions were produced through diazonium-mediated radical coupling of the two linkers **L1** and **L2** to the surfaces of DND particles in dispersion to give **DND-L1** and **DND-L2**. These particles were extensively characterized with respect to surface loading (~0.3 mmol g^{-1}), colloidal properties ($\zeta = +40$–50 mV at pH 6) and surface chemistry (FTIR/Raman, cf. Supporting Information, Chapter S2.2). CuAAC ligation of **Ru1-C≡CH** was achieved over the course of several days to yield the ruthenium functionalized nanodiamond dispersions **DND-L1-Ru1** and **DND-L2-Ru1**. Characterization through an extensive suite of methods for both conjugates was performed, including UV–vis absorption, FTIR and X-ray photoelectron (XPS) spectroscopies, as well dynamic light scattering (DLS), thermogravimetric analysis (TGA) and elemental analysis (EA). Representative analyses of **DND-L2-Ru1** are shown in Figure 2, with the full data set provided in the Supporting information (Chapter S3 of the Supporting Information).

UV-Visible absorption and FTIR spectroscopy demonstrate the retention of optical and structural characteristics of the ruthenium photosensitizer following DND attachment, with a slight bathochromic shift (~17 nm / 795 cm^{-1}) in the ^{3}MLCT ascribed transition upon DND attachment observed for both systems irrespective of linker conjugation. Ruthenium-functionalized **DND** dispersions demonstrated good colloidal stability, presumably because of a conserved positive surface charge ($\zeta = +19$-24 mV at ~pH 6). The observed particle sizes (D_{50} values typically between 60–80 nm) in water even after prolonged storage times confirm the good colloidal stabilization. These dispersions have also been used to coat boron-doped diamond electrodes for photoelectrocatalytic experiments, ensuring a homogeneous distribution of the particles on the electrode surface (see below Figure S30g,h).

Deconvoluted C1s regions of XPS spectra demonstrated a pattern of C1s environments representing both core sp^3 (C1s-1), surface sp^3 (C1s-2), C-O (C1s-3) and C = O (C1s-4/5) environments in agreement with published literature values for other functionalized carbon materials [62,63]. XPS spectra also demonstrated notable peaks around 282 eV, characteristic of the 3d 5/2 component of ruthenium in a +II oxidation state, further confirming attachment of the ruthenium complexes to the surface (cf. Supporting Information, Chapter S3.5) [54].

Quantitative elemental analysis of relevant DND species revealed nitrogen/ruthenium content ratios around 8–9:1 when corrected for core nitrogen content exhibited by the milled DND (**mDND**).

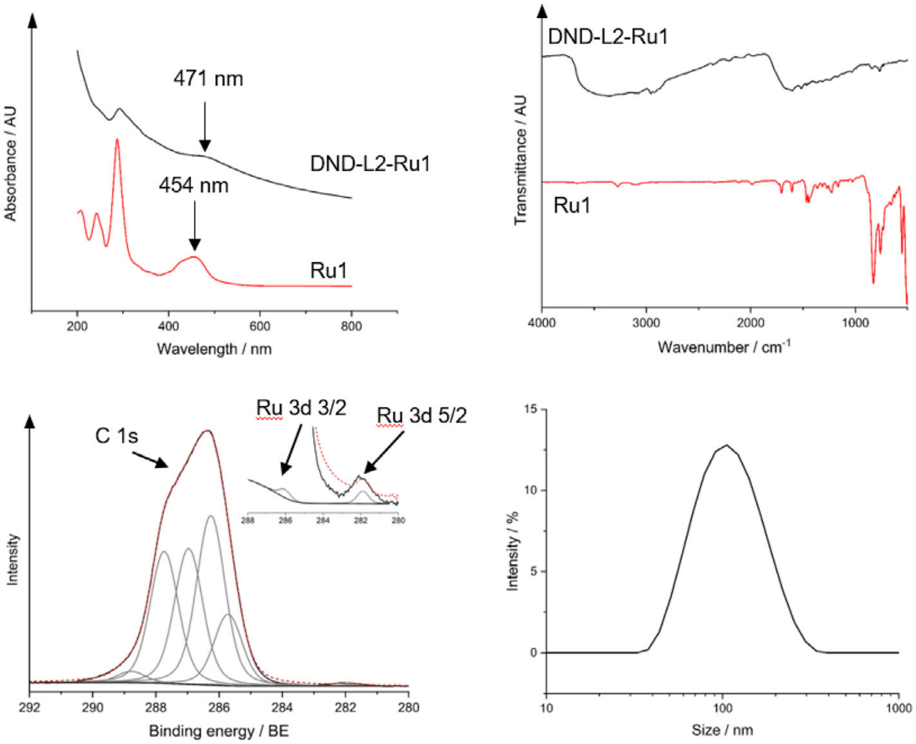

FIGURE 2 | Spectroscopic characterization **of DND-L2-Ru1**; Top left: UV–vis spectra of **Ru1** (red) and **DND-L2-Ru1** (black). Top right: FTIR spectra of **Ru1** (ATR, red) and **DND-L2-Ru1** (DRIFTS, black), Bottom left: deconvoluted XPS spectrum of **DND-L2-Ru1** (insert: magnified region from 280–284 eV showing Ru 3d 3/2 shoulder and Ru 3d 5/2 peak), Bottom right: DLS particle size analysis of an aqueous dispersion of **DND-L2-Ru1** (D10: 38.9 nm, D50: 74.6 nm, D90: 374 nm).

This reflects the nitrogen:ruthenium ratio exhibited in the triazole-linked **Ru-1** complex on DND, supporting aforementioned spectroscopic data suggesting conserved coordination geometry for **Ru1** (see Supporting Information, Chapter S3.5.2).

The colloidal stability, surface loading and optical properties of the **DND-Ru1** conjugates were retained following irradiation under UV light for all particle dispersions (cf. Supporting Information, Chapter S9) proving photostability under conditions utilized for the emission of electrons applicable in photoelectrocatalytic experiments. Additionally, we performed elemental and XPS analysis before and after illumination with a Hg/Xe lamp in $KHCO_3$ solution and under applied bias confirmed the retention of the ruthenium-functionalized particles on the coated electrode surface under the relevant reaction conditions (Figure S30 and Table S8).

The electronic properties and band edge/frontier molecular orbital relationship of diamond and ruthenium photosensitizer of ruthenium-functionalized **mDND** particles were investigated with X-ray absorption spectroscopy and ultraviolet absorption spectroscopy, with accompanying insight into the frontier molecular orbital structure based on theoretical calculations.

2.2 | Energy Alignment and Charge Transfer Between the DND and Dye in Water

To better understand charge excitation and electronic transfer processes in the system, we combine ultraviolet photoelectron spectroscopy (UPS) and X-ray absorption spectroscopy (XAS) under vacuum to determine the alignment between the occupied and unoccupied electronic states of the Ru dye and the DND. Additionally, XAS measurements in water are used to probe the new electronic equilibrium established after charge transfer with the electrolyte. Upon immersion in water, equilibration between the Fermi level of the dye/DND system and the chemical potential of the electrolyte leads to charge redistribution, which can modify orbital occupations and influence subsequent photoinduced excitations and charge transfer processes.

The position of occupied electronic states was derived by UPS shown in Figure 3b (and in more detail in Figure S13). For the **Ru1** complex, three electronic states at 2.1, 3.7, and 5.5 eV below the Fermi level of a gold reference (E_F^{Au}) are identified. The HOMO level is attributed to a metal centered molecular orbital and is found at the same energy as in previous work on $Ru(bpy)_3$ complexes [64]. On **DND-L2-Ru1**, the HOMO level is shifted to 1.9 eV (−0.2 eV compared to **Ru1**), which may result from the electronic conjugation with the DND.

The partial density of unoccupied electronic states was determined by XAS at the C K edge measured in vacuum shown in Figure 3a. The XAS of **DND-L1-Ru1** and non-functionalized hydrogenated DNDs (**DND-H**) are shown in Figure S11. **DND-H** and both Ru-functionalized samples exhibit a rising edge after 287 eV having contribution from core excitation to surface states (C-H and C-OH) up to a maximum around 289.5 eV corresponding to the conduction band minimum (CBM) as also found on single crystal diamond and **DND-H** [62]. The XA

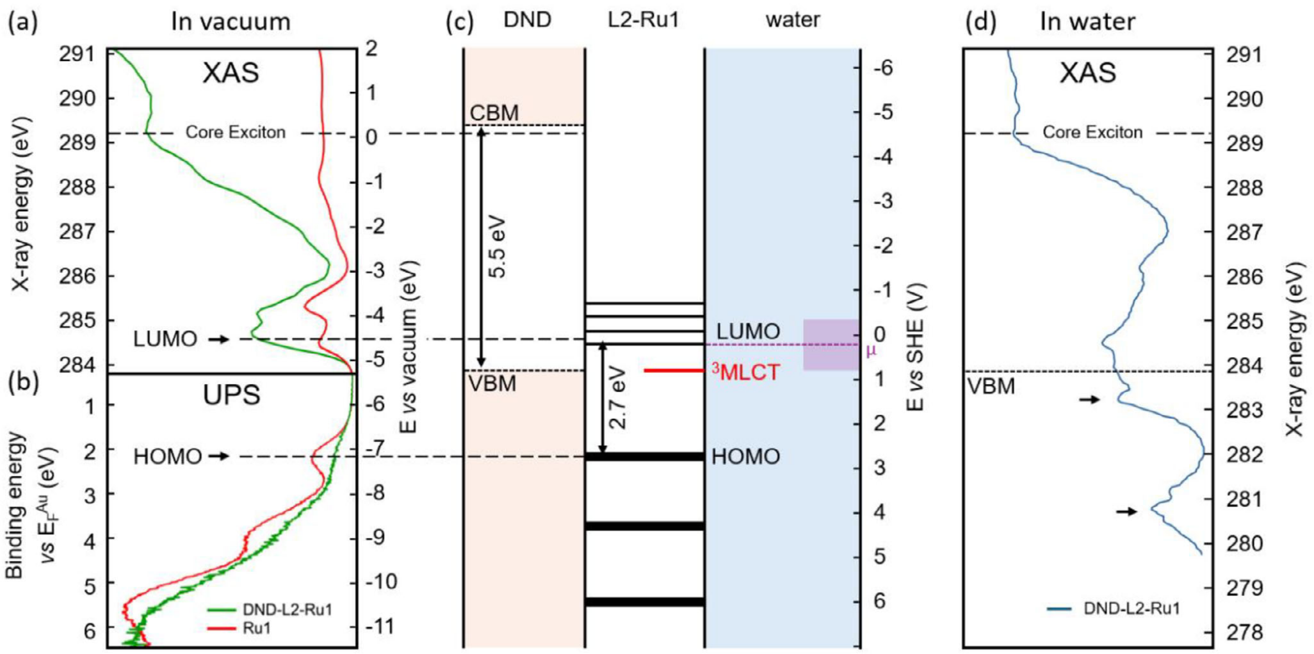

FIGURE 3 | Experimental determination of the band alignment. (a) XAS at the C K edge and (b) UPS of conjugated DND-L2-Ru1 (green) and Ru1 (red) in vacuum. XAS and UPS are shown on a unified energy scale (left) to allow an alignment of the energy levels to the vacuum level (right). (c) Band alignment scheme of the DND-L2-Ru1 with the position of the VBM and HOMO determined by UPS and CBM and LUMO determined by the XAS in vacuum. The ^{3}MLCT state obtained from UV–vis is also indicated (red). The electrochemical stability window of water at pH 7 is indicated in purple showing that at equilibrium, the ^{3}MLCT state is populated. (c) XAS in water of DND-L2-Ru1 measured in Total Ionic Yield. In contrast to vacuum measurements, additional unoccupied electronic states are detected in the DND valence band (black arrows), which are interpreted in terms of electron transfer to the conjugated dye.

spectrum of free **Ru1** exhibits a doublet at 285.0 and 285.8 eV. Time dependent Density Functional Theory (TD-DFT) studies suggest this double peak feature originates from distinct chemical environments of carbon atoms (carbon bonded to another carbon or a nitrogen atom) within the ligand architecture of the **Ru1** complex (cf. Supporting Information), representing the two lowest lying unoccupied molecular orbitals (LUMO and LUMO+1) shown in Figure 3a. The XA spectra for **DND-L2-Ru1** shows an additional shoulder at 286.2 eV, that is absent in **DND-L1-Ru1**, which we attribute to an additional charge transfer state induced by the conjugation in the linker, supporting a linker-dependent regime of coupling. In the following, we focused on the conjugated linker system, **DND-L2-Ru1** due to this observation.

The energy level scheme of the **DND–L2–Ru1** complex is shown on the right side of Figure 3c. The VBM of the DND is estimated from UPS at 0.2 eV below the E_F of the gold reference (cf. Supporting Information) and provides the absolute position of the Ru dye's HOMO. The XAS spectrum is aligned using the core exciton of diamond, as previously reported [65] and considering a bandgap of 5.5 eV. The energy of the core-hole exciton at the C1s was estimated to be 0.2 eV for diamond [66] and 0.5 eV for C_{60} [67]. As no value was reported so far for DND to our knowledge, we speculate that it is to be expected between these two values. A slight NEA of −0.3 eV of the **DND-L2-Ru1** is estimated from this energy level alignment, slightly below the value reported on hydrogen terminated DND (-0.8 eV) [68], most likely due to the removal of some hydrogenated groups upon functionalization. The resulting positions of the HOMO and LUMO of the Ru1 dye are consistent with their known energy gap (2.7 eV), further supporting the accuracy of this alignment. The ^{3}MLCT state (shown in red) is not observed in the UPS as it is unoccupied nor in the C K-edge XAS, as it corresponds to excitation on the metal center, but it can be placed relative to the dye's HOMO and LUMO. In vacuum, the Fermi level of the system is pinned by charge transfer between the DND and the attached dye, lying between the HOMO and the unoccupied ^{3}MLCT state—very close to the DND's VBM [69]. However, when put in water, charge transfer can occur between the DND, the dye and water. In water, the chemical potential represented in purple in Figure 3c lies above the ^{3}MLCT state. It is likely that charge transfer in the system in water leads to the population of this state [41].

The effect of solvation and charge transfer on the electronic structure of the DND can be observed on the C K-edge XAS of the **DND-L2-Ru1** characterized directly in water in Figure 3d. To this aim, Total Ionic Yield (TIY) XAS detection was used (see Figures S14–S16). Interestingly, the unoccupied electronic states in the pre-edge region appear strongly affected by aqueous solvation. The peak at 286.5 eV corresponding to the C = O surface groups appears more pronounced, probably related to the NDs surface oxidation in water under X-ray light. Some unoccupied electronic states are observed at 281 eV, for energies in the valence band of the diamond. Similar observations have been made on DNDs dispersed in water and were interpreted by the formation of valence holes following the charge transfer to the water molecules [70]. The two absorption peaks of the ligand, that are clearly observed in vacuum, are replaced by a large absorption band between 283.3 and 286 eV and the unoccupied states 1.5 eV below the measurements in vacuum align with the ^{3}MLCT state of the

Ru dye. We interpret these as charge transfers from the DND to the dye populating the ^{3}MLCT state similar to the charge transfer of the DNDs in water leading to the formation of valence holes.

Additionally, TIY-XAS at the O K edge was used to study the immediate environment of the diamond surface. This method probes mostly the interfacial water in the vicinity of the **DND-L2-Ru1** (Figure S15). The XAS at the O K edge is highly sensitive to the water hydrogen bonding. Interestingly, the electronic structure of the interfacial water resembles water confined within porous carbon [71] rather than interfacial water around dispersed DNDs [72]. This suggests that the water contained in DNDs-based thin films has a different hydrogen bonding than dispersed DNDs likely due to confinement.

The electron transfer from the DND to the dye observed through the in situ measurement of XAS is coherent with previous findings. Dye sensitized diamonds studied previously report hole donation from ruthenium dye to the diamond in case of B-doped diamond films, where the HOMO of the dye is located below the VBM of diamonds resulting in improved photocurrents evidenced through photochemical experiments [54]. However, these measurements also suggest that the populated ^{3}MLCT state state of the dye can be photoexcited. To demonstrate this photoexcitation, we performed transient absorption spectroscopy (TAS).

2.3 | Photoexcitation and Charge Transfer Dynamics

In order to probe possible charge transfer manifolds exhibited by **DND-L2-Ru1**, TAS of this sample was compared to bare **DND-H** and the **Ru1** complex alone under deep UV (DUV, 225 nm) excitation (Figure 4). DUV excitation was chosen to ensure one-photon band-to-band excitation of electrons above the VBM, which ensure the emission of solvated electrons from the DNDs [60]. In contrast to bare **DND** and **Ru1**, the TA signal is stronger and notably shows a dip centered around 585 nm (17 100 cm^{-1}, 2.12 eV). This feature cannot be assigned to a ground state absorption of the DND-Ru complexes as it does not relate to any absorption band in the UV–vis steady–state absorption spectra (Figure 2). Furthermore, since both fluorescence and phosphorescence signals have been reported for Ru(bpy)$_3$ with much longer lifetimes, we attribute this observation to stimulated emission [73,74].

In comparison to time-resolved spectroscopy of spontaneous emission, we ascribed the emissive state at 585 nm to the ^{3}MLCT state of Ru(bpy)$_3$ [73,75]. By comparing kinetic traces averaged within and outside the dip region, a decay of the stimulated emission signal within 2 ps is observed, contrasting with that observed for bare DND. Followed by an apparent recovery until about 10 picoseconds, the signal then decays in a manner similar to the positive signal from the other spectral region of the **DND-L2-Ru1** trace. The overarching decay observed on the longer timescale (ns) is similar to that observed for DND and NaI solutions [76,77], likely due to diffusion-driven recombination of solvated electrons with ionized DNDs [47]. The fast-decaying stimulated emission signal, however, is absent in both DNDs and in **Ru1**. In the latter, both TA and spontaneous emission signals are observed with lifetimes of several hundred nanoseconds [73,74]. We attribute the stimulated emission to the excitation of HOMO electrons generating holes, which are filled by the deexcitation of the populated ^{3}MLTC level (see scheme Figure 4c). It starts very early as the level is already populated and likely destabilized by the binding configuration with the diamond. Its fast decay is possibly due to charge-transfer processes between the **DND** and **Ru1** [75], whereby either or both of the partners may be in a vibronically excited state.

The ^{3}MLCT state can be both populated and further excited to generate solvated electrons. Photocurrent measurements, presented in the Figure 4d for a BDD electrode decorated with **DND–L2–Ru1**, reveal a sub-bandgap photocurrent onset at approximately 3.2 eV or 385 nm coincides with the appearance of catalytic activity (Table 1) and the emission of solvated electrons (Figure S17). At this wavelength, the photocurrent scales with the square root of the irradiance (Figure 4e), indicating a single-photon excitation process where the steady-state carrier density is limited by bimolecular recombination under high photon flux. The excitation threshold of 3.2 eV corresponds to promotion of the ^{3}MLCT state into surface states of the diamond, which align with the redox potential of solvated electrons, as demonstrated by the blue arrow in Figure 4c. This alignment, previously determined by X-ray spectroscopy (Figure 3), suggests that solvated electron emission originates from photoexcitation of the dye's ^{3}MLCT state into DND surface states located above the redox potential of solvated electrons. In this mechanism, the dye transfers an electron to the DND. The transfer from dye to DND is facilitated by strong orbital delocalization of **Ru1** through the **L2** linker. Evidence for such coupling is provided by the XAS spectrum (Figure 3a), which displays new unoccupied states near 285.7 eV that are absent in the spectra of the isolated dye or DND (see Figure S11). Once injected into the electrolyte, the electrons rapidly relax to the redox potential characteristic of solvated electrons, while the hole in the dye is refilled via the DND, whose valence-band maximum aligns with the ^{3}MLCT state, either through sacrificial electron donors in solution or through electrical contact with the electrode. Overall, the DNDs act both as electron donors to the dye and as emitters of solvated electrons, thereby enabling visible-light-driven solvated-electron emission.

2.4 | Photoelectrocatalytic CO_2 Reduction as a Proof-of-Concept

As a proof of concept, pristine **mDND** (extensively cleaned through multiple mineral acid and oxidation steps to eliminate any possible metal contamination, Table S9) and **Ru1**-functionalized DND film cathodes produced by coating a conductive, polycrystalline diamond substrate with the respective nanodiamond particles (see Supporting Information for details) were compared for their performance in photoelectrochemical CO_2 reduction in 0.5 M $KHCO_3$ (aq). The electrolyte was first purged with N_2 for 30 min and subsequently saturated with CO_2 for 1 h prior to electrochemical experiments. CO_2 flow was continued during reaction to maintain saturation during the experiment. UV irradiation of the cathode was performed with a 500 W Hg(Xe) arc lamp source. Current responses during CV of the DND film electrodes are presented in Figure 5.

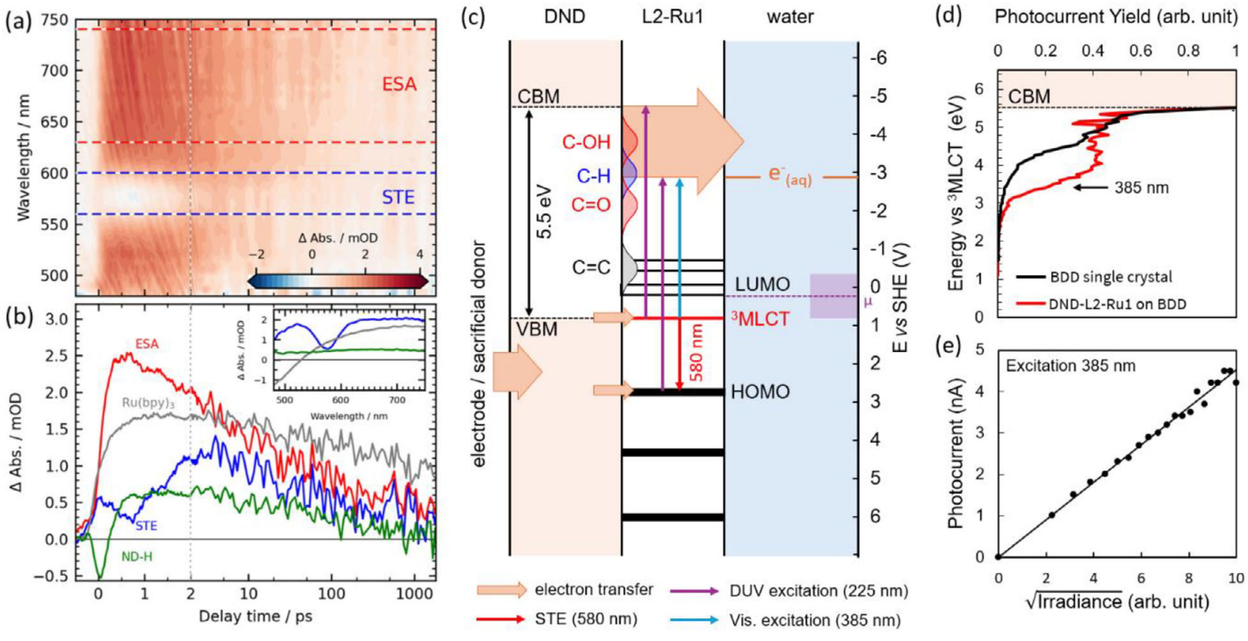

FIGURE 4 | Charge excitation and emission pathways of solvated electrons. (a) Spectro-temporal map of the transient absorption (TA) of DND-L2-Ru1 under DUV excitation (225 nm). Red (blue) regions correspond to positive (negative) absorption changes. (b) Kinetic traces compared with Ru1 and H-DND, averaged over spectral ranges inside the dip (blue, "STE") and outside the dip (red, "ESA"). The inset shows the corresponding averaged TA spectra integrated over 0–3 ps. (c) Band alignment of DND with the L2-Ru1 electronic states and the electrolyte, as determined experimentally in Figure 3, illustrating the charge transfer processes populating the ^{3}MLCT state. Photoexcitation arrows are drawn to scale. Excitation at 225 nm (purple arrow) promotes electrons from the HOMO to DND surface states, leading to the observed STE from the ^{3}MLCT state (red arrow). (d) Photocurrent spectra of a reference single-crystal BDD (black) and BDD decorated with DND-L2-Ru1, showing charge emission upon excitation at 385 nm, corresponding to visible-light excitation of the ^{3}MLCT state (blue arrow in panel c). (e) Linear dependence of the photocurrent at 385 nm on the square root of the irradiance, suggesting a charge-transfer-limited mechanism.

TABLE 1 | Formate production in in aqueous $KHCO_3$ solution and two ionic liquid systems with Ru modified and non-modified **mDND**-OBDD electrodes.

Electrolyte	Electrode material/catalyst	Formate production / μmol cm^{-2} h^{-1}
0.5 M $KHCO_3$ [a]	**mDND**-BDD	0.04
	DND-L2-Ru1-BDD	0.06
	DND-L1-Ru1-BDD	0.09
N_{1114}BTA[b]	**mDND**-BDD	0.42
	DND-L2-Ru1-BDD	0.76
	DND-L1-Ru1-BDD	0.74
N_{1123}BTA[b]	**mDND**-BDD	0.31
	DND-L2-Ru1-BDD	0.56
	DND-L1-Ru1-BDD	0.58

[a] 0.5 M in H2O, at −1.2 V with CO2 flow under UV illumination for 1 h.
[b] 3:1 IL:DMSO, at −1.7 V with CO2 flow under solar illumination for 1 h.

In Figure 5a for **mDND** coated electrodes very little current response is seen except at potentials below −1.2 V in the presence of N_2 and CO_2 which is likely due to the hydrogen evolution reaction (HER). In contrast, in Figure 5b for the **DND-L2-Ru1** functionalized electrode enhanced reduction currents are observed in the presence of CO_2 compared to N_2 with a potential onset of ca. −0.8 V vs. Ag/AgCl. This indicates spectroelectrocatalytic CO_2 reduction is occurring at the **DND-L2-Ru1** modified electrode.

To investigate this further, NMR analysis of the liquid phase after chronoamperometric experiments was carried out in aqueous

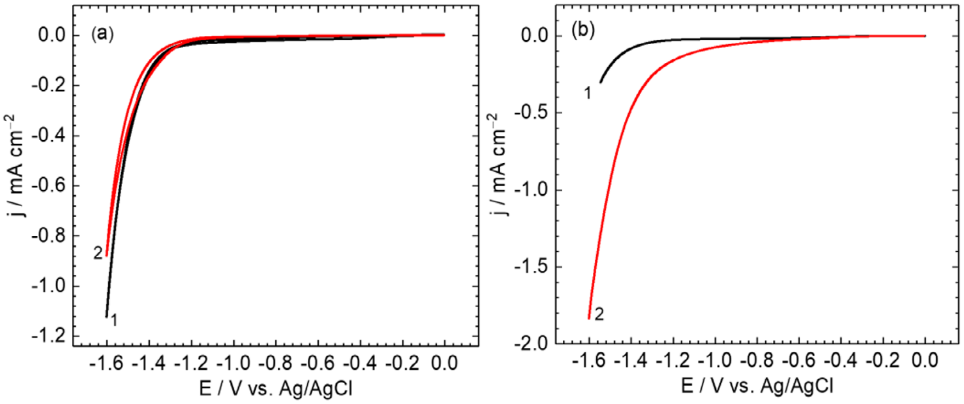

FIGURE 5 | CVs of (a) **mDND** and (b) **DND-L2-Ru1** modified BDD electrodes in N_2 (black 1) and CO_2 (red 2) saturated $KHCO_3$ under UV irradiation using a 500 W Hg(Xe) arc lamp.

(0.5 M $KHCO_3$) and ionic liquids (ILs) to detect the presence of CO_2 reduction products, which showed the presence of formate as the predominant reaction product. Small amounts of methanol have been also detected, however not in amounts quantifiable with the applied methods. Future optimization of the diamond based photocatalysis will require an in-depth analysis of byproducts and competing reaction pathways such as hydrogen evolution. Catalysis experiments were performed under significantly negative potentials, to inhibit photo-induced diamond oxidation and to optimize the optical response (based on the results in Figure 5). We were limited in the aqueous electrolyte to –1.2 V due to the overriding HER observed at more negative potentials, however IL systems were able to be subjected to –1.7 V. A large number of samples were investigated for CO_2 reduction activity including the bare diamond substrate, substrates with DND coatings in the absence of Ru, and the Ru-functionalized DND coated electrodes. Typical general data are shown in Table S7, where it can be seen that oxygen terminated bare diamond substrates in aqueous media show virtually no activity for CO_2 reduction. As a consequence, significant observation of catalytic activity can be attributed to the surface modifications used. Specific results of pertinence to the current work are shown in Table 1. Regarding the UV-stability of the Ru-functionalized particles **DND-L1-Ru1** and **DND-L2-Ru1**, after 1 h irradiation with the UV lamp in aqueous dispersion without any gas saturation the supernatant was analyzed by NMR spectroscopy and ESI mass spectrometry. Neither method showed any decomposition of the Ru-complex or the linker system. Although the dispersions heated up by ~20°C, no aggregation took place (cf. Table S6).

The detection limits of the formate reaction product both in $KHCO_3$ (aq) and in ILs in our NMR analyses are approximately 0.01 µmol cm^{-2} h^{-1} and no formate is observed at this limit of detection in the dark for oxidized diamond electrodes coated with **DND** (cf. Supporting Information, chapter 10). Under UV illumination, however, some activity was observed in experiments with **mDND** coated electrodes and was further increased with addition of **DND-L1-Ru1** and **DND-L2-Ru1** onto BDD electrodes, consistent with previous TA experiments [60]. Both the increased surface area of the coated nanodiamond particles and the strong electronic coupling of nanodiamond and the attached ruthenium complexes enhance the catalytic activity. A significant improvement in CO_2 reduction was obtained in experiments in IL media **N_{1114}BTA** and **N_{1123}BTA**, (Figure S21) due to the increased solubility of CO_2 in these solvents and applied potential. The results obtained in specifically selected ILs with Ru modified and non-modified **mDND**–BDD electrodes are presented in the Table 1. Significantly improved reactivity is now seen, enabling reaction products to be easily detected even under solar radiation rather than UV.

According to the results presented in Table 1, the best activity was observed in N_{1114}BTA with both Ru-modified nanodiamonds **DND-L1-Ru1** and **DND-L2-Ru1** dropcoated on BDD electrodes. The electrodes modified with mDND without Ru, (m**DND**-BDD), show in both ILs much lower activity. Compared to the experiments with $KHCO_3$ (aq), where activity observed under solar irradiation was very low (<0.05 µmol cm^{-2} h^{-1} of formate produced), much better performance was detected in experiments with ILs, where the amount of product obtained was almost 10 times higher. These results suggest that it is possible to move from UV to solar irradiation if ILs are used. The performance in ILs is similar for both types of linkers, non-conjugated (**L1**) and conjugated (**L2**), and much higher than in aqueous media. In ILs, yield of formic acid is on average nearly two times higher than that of non-functionalized DND. The main reason for this increase lies in the significantly increased solubility of CO_2 in these ionic liquids [78,79].

Comparison of the results obtained with other work shows activity levels seen here (Table 1) are comparable or greater than the circa max. 0.2–0.3 µmol h^{-1} cm^{-2} CO_2 reduction rates reported for nanodiamond suspensions or solid electrodes [6,45,80]. This confirms that the control over reaction rates observed with the Ru catalysts seen here is of significance in the general field of CO_2 reduction at diamond surfaces even without optimization of the photocatalytic system. Based on our findings regarding the energy level structure of diamond functionalized with a suitable sensitizer, we will explore the photocatalytic activity of such diamond-conjugates in future work.

3 | Conclusions

In summary, we introduce here a tailored functionalized diamond nanomaterial with suitable intrabandgap states that enable the generation of solvated electrons upon visible excitation. The spectroscopic investigations using UPS, XAS and TAS of ruthenium-functionalized nanodiamond indicate significant electronic conjugation between the ruthenium based surface moieties and the diamond, supporting a photosensitization based system. The emission of solvated electrons from these conjugates was proven by TAS. As a proof of concept, solar-driven CO_2 photoelectrocatalytic reduction using this nanodiamond based system based on a dye to diamond PET transfer process is demonstrated for the first time. Reaching photoelectrocatalytic yields of up to 0.76 μmol cm^{-2} h^{-1} under solar illumination at −1.7 V, these results demonstrate the principal applicability and represent a significant step in the development of novel diamond based reductive photoelectrocatalytic systems. In confirming the feasibility of solar CO_2 reduction, this work opens the route to the development of scalable, sustainable strategies through further photosensitizer development and reactor design. Future research will be driven toward other, more benign sensitizers. The ultimate goal of photocatalysis in aqueous electrolytes, will require additional efforts also in reactor design, such as increasing the CO_2 pressure and/or using thin liquid falling film reactors as potential avenues for further development.

Acknowledgements

This research was supported by the European Commission under the Horizon 2020 framework (Grant number 665085, DIACAT). Additionally, AK thanks the BMBF for support under project CarbonCat (Grant No. 033RC009B) and the DFG for support in the priority program SPP2370 (Grant No. 501934692). The authors thank Mario Borgwardt, Iain Wilkinson and Igor Kiyan for access and technical assistance with the ULLAS femtosecond laser facility at Helmholtz-Zentrum Berlin. The authors also acknowledge the kind support from Jian Ren, Louis Godeffroy and the staff of the BESSY II synchrotron facility, especially Ronny Golnak and Jie Xiao. The authors thank the Helmholtz-Zentrum Berlin for the allocation of beamtime at the U49/2 PGM-1 synchrotron beamline at BESSY II. AK and AHD thank Martin Kamp and Johannes Ackermann for support with TEM.

Open access funding enabled and organized by Projekt DEAL.

Conflicts of Interest

The authors declare no conflicts of interest.

Data Availability Statement

The data that support the findings of this study are available from the corresponding authors upon reasonable request.

References

1. X. Min and M. W. Kanan, “Pd-Catalyzed Electrohydrogenation of Carbon Dioxide to Formate: High Mass Activity at Low Overpotential and Identification of the Deactivation Pathway,” *Journal of the American Chemical Society* 137 (2015): 4701–4708.

2. N. Ikemiya, K. Natsui, K. Nakata, and Y. Einaga, “Long-Term Continuous Conversion of CO_2 to Formic Acid Using Boron-Doped Diamond Electrodes,” *ACS Sustainable Chemistry & Engineering* 6 (2018): 8108–8112.

3. K. Natsui, H. Iwakawa, N. Ikemiya, K. Nakata, and Y. Einaga, “Stable and Highly Efficient Electrochemical Production of Formic Acid From Carbon Dioxide Using Diamond Electrodes,” *Angewandte Chemie International Edition* 57 (2018): 2639–2643.

4. R. J. Lim, M. Xie, M. A. Sk, et al., “A Review on the Electrochemical Reduction of CO_2 in Fuel Cells, Metal Electrodes and Molecular Catalysts,” *Catalysis Today* 233 (2014): 169–180.

5. M. Tomisaki, S. Kasahara, K. Natsui, N. Ikemiya, and Y. Einaga, “Switchable Product Selectivity in the Electrochemical Reduction of Carbon Dioxide Using Boron-Doped Diamond Electrodes,” *Journal of the American Chemical Society* 141 (2019): 7414–7420.

6. L. Zhang, D. Zhu, G. M. Nathanson, and R. J. Hamers, “Selective Photoelectrochemical Reduction of Aqueous CO_2 to CO by Solvated Electrons,” *Angewandte Chemie International Edition* 53 (2014): 9746–9750.

7. S. A. Yao, R. E. Ruther, L. Zhang, R. A. Franking, R. J. Hamers, and J. F. Berry, “Covalent Attachment of Catalyst Molecules to Conductive Diamond: CO_2 Reduction Using “Smart” Electrodes,” *Journal of the American Chemical Society* 134 (2012): 15632–15635.

8. Y. Hori, H. Wakebe, T. Tsukamoto, and O. Koga, “Electrocatalytic Process of CO Selectivity in Electrochemical Reduction of CO_2 at Metal Electrodes in Aqueous Media,” *Electrochimica Acta* 39 (1994): 1833–1839.

9. P. Chen, Y. Zhang, Y. Zhou, and F. Dong, “Photoelectrocatalytic Carbon Dioxide Reduction: Fundamental, Advances and Challenges,” *Nano Materials Science* 3 (2021): 344–367.

10. S. Xie, Q. Zhang, G. Liu, and Y. Wang, “Photocatalytic and Photoelectrocatalytic Reduction of CO_2 using Heterogeneous Catalysts With Controlled Nanostructures,” *Chemical Communications* 52 (2015): 35–59.

11. E. E. Barton, D. M. Rampulla, and A. B. Bocarsly, “Selective Solar-Driven Reduction of CO_2 to Methanol Using a Catalyzed p-GaP Based Photoelectrochemical Cell,” *Journal of the American Chemical Society* 130 (2008): 6342–6344.

12. P. K. Jiwanti, K. Natsui, K. Nakata, and Y. Einaga, “Selective Production of Methanol by the Electrochemical Reduction of CO_2 on Boron-Doped Diamond Electrodes in Aqueous Ammonia Solution,” *RSC Advances* 6 (2016): 102214–102217.

13. R. De, S. Gonglach, S. Paul, et al., “Electrocatalytic Reduction of CO_2 to Acetic Acid by a Molecular Manganese Corrole Complex,” *Angewandte Chemie International Edition* 59 (2020): 10527–10534.

14. E. E. Benson, C. P. Kubiak, A. J. Sathrum, and J. M. Smieja, “Electrocatalytic and Homogeneous Approaches to Conversion of CO_2 to Liquid Fuels,” *Chemical Society Reviews* 38 (2008): 89–99.

15. J. Albero, Y. Peng, and H. García, “Photocatalytic CO_2 Reduction to C^{2+} Products,” *ACS Catalysis* 10 (2020): 5734–5749.

16. D. D. Zhu, J. L. Liu, and S. Z. Qiao, “Recent Advances in Inorganic Heterogeneous Electrocatalysts for Reduction of Carbon Dioxide,” *Advanced Materials* 28 (2016): 3423–3452.

17. Q. Lu, J. Rosen, Y. Zhou, et al., “A Selective and Efficient Electrocatalyst for Carbon Dioxide Reduction,” *Nature Communications* 5 (2014): 3242.

18. S. Ma, Y. Lan, G. M. J. Perez, S. Moniri, and P. J. A. Kenis, “Silver Supported on Titania as an Active Catalyst for Electrochemical Carbon Dioxide Reduction,” *Chemsuschem* 7 (2014): 866–874.

19. W. Cai, X. Cao, Y. Wang, S. Chen, J. Ma, and J. Zhang, “Spatial Structure of Electron Interactions in High-entropy Oxide Nanoparticles for Active Electrocatalysis of Carbon Dioxide Reduction,” *Advanced Materials* 36 (2024): 2409949.

20. J. Yu, J. González-Cobos, F. Dappozze, P. Vernoux, A. Caravaca, and C. Guillard, “Basic Comprehension and Recent Trends in Photoelectrocatalytic Systems,” *Green Chemistry* 26 (2024): 1682–1708.

21. I. Ahmad, Y. Zou, J. Yan, et al., “Semiconductor Photocatalysts: A Critical Review Highlighting the Various Strategies to Boost the Photocatalytic Performances for Diverse Applications,” *Advances in Colloid and Interface Science* 311 (2023): 102830.

22. Z. Chen, G. Zhang, S. Cao, et al., “Advanced Semiconductor Catalyst Designs for the Photocatalytic Reduction of CO_2,” *Materials Reports Energy* 3 (2023): 100193, https://doi.org/10.1016/j.matre.2023.100193.

23. S. Yao, J. He, F. Gao, et al., "Highly Selective Semiconductor Photocatalysis for CO_2 Reduction," *Journal of Materials Chemistry A* 11 (2023): 12539–12558.

24. G. M. Swain and R. Ramesham, "The Electrochemical Activity of Boron-Doped Polycrystalline Diamond Thin Film Electrodes," *Analytical Chemistry* 65 (1993): 345–351.

25. J. Ristein, W. Stein, and L. Ley, "Photoelectron Yield Spectroscopy on Negative Electron Affinity Diamond Surfaces: A Contactless Unipolar Transport Experiment," *Diamond and Related Materials* 7 (1998): 626–631.

26. P. Ashcheulov, J. Sebera, A. Kovalenko, et al., "Conductivity of Boron-Doped Polycrystalline Diamond Films: Influence of Specific Boron Defects," *The European Physical Journal B* 86 (2013): 443.

27. D. Takeuchi, H. Kato, G. S. Ri, et al., "Direct Observation of Negative Electron Affinity in Hydrogen-Terminated Diamond Surfaces," *Applied Physics Letters* 86 (2005): 152103.

28. K. M. O'Donnell, M. T. Edmonds, J. Ristein, et al., "Diamond Surfaces With Air-Stable Negative Electron Affinity and Giant Electron Yield Enhancement," *Advanced Functional Materials* 23 (2013): 5608–5614.

29. N. Yang, A. Krueger, and R. J. Hamers, "Diamond Chemistry: Advances and Perspectives," *Angewandte Chemie International Edition* 64 (2025): 202418683.

30. N. Nunn, M. Torelli, G. McGuire, and O. Shenderova, "Nanodiamond: A High Impact Nanomaterial," *Current Opinion in Solid State and Materials Science* 21 (2017): 1–9.

31. Irkham, S. Nagashima, M. Tomisaki, and Y. Einaga, "Enhancing the Electrochemical Reduction of CO_2 by Controlling the Flow Conditions: An Intermittent Flow Reduction System With a Boron-Doped Diamond Electrode," *ACS Sustainable Chemistry & Engineering* 9 (2021): 5298–5303.

32. S. Yu, N. Yang, S. Liu, and X. Jiang, "Electrochemical and Photochemical CO_2 Reduction using Diamond," *Carbon* 175 (2021): 440–453.

33. S. Lips, D. Schollmeyer, R. Franke, and S. R. Waldvogel, "Regioselective Metal- and Reagent-Free Arylation of Benzothiophenes by Dehydrogenative Electrosynthesis," *Angewandte Chemie International Edition* 57 (2018): 13325–13329.

34. Y. Einaga, "Boron-Doped Diamond Electrodes: Fundamentals for Electrochemical Applications," *Accounts of Chemical Research* 55 (2022): 3605–3615.

35. M. Augustín, V. Vyskočil, O. Szabó, et al., "Pilot Study of Electrochemical Reduction of Selected Nucleotides and Double-Stranded DNA at Pristine Micro-/Ultrananocrystalline Boron-Doped Diamond Electrodes at Very Negative Potentials," *Electrochimica Acta* 514 (2025): 145549.

36. W. Yang, Z. Deng, Y. Wang, et al., "Porous Boron-Doped Diamond for Efficient Electrocatalytic Elimination of Azo Dye Orange G, Separation Purif," *Technol* 293 (2022): 121100.

37. G. Liu, C. Feng, and P. Shao, "Degradation of Perfluorooctanoic Acid With Hydrated Electron by a Heterogeneous Catalytic System," *Environmental Science & Technology* 56 (2022): 6223–6231.

38. Y. M. Hunge, T. Inaba, K. Ishihara, et al., "Electrochemical Carboxylation: Green Synthesis of Atrolactic Acid using Boron-Doped Diamond Electrodes," *Electrochimica Acta* 509 (2025): 145310.

39. A. Tariq, M. Z. Akram, M. D. Ghouri, et al., "Recent Progress on Boron-Doped Diamond Electrodes for Electrochemical CO_2 Reduction: A Mini-Review," *Energy & Fuels* 38 (2024): 10445–10455.

40. M. C. James, A. Croot, P. W. May, and N. L. Allan, "Negative Electron Affinity From Aluminium on the Diamond (1 0 0) Surface: A Theoretical Study," *Journal of Physics: Condensed Matter* 30 (2018): 235002.

41. A. Chemin, L. Godeffroy, M. Rusu, et al., "Modulating Surface Redox Reactions and Solvated Electron Emission on Boron-Doped Diamond by (Photo)Electrochemistry," *PRX Energy* 4 (2025): 033011.

42. S. Trasatti, "The Absolute Electrode Potential: An Explanatory Note (Recommendations 1986)," *Pure and Applied Chemistry* 58 (1986): 955–966.

43. R. J. Hamers, J. A. Bandy, D. Zhu, and L. Zhang, "Photoemission From Diamond Films and Substrates Into Water: Dynamics of Solvated Electrons and Implications for Diamond Photoelectrochemistry," *Faraday Discussions* 172 (2014): 397–411.

44. D. Zhu, L. Zhang, R. E. Ruther, and R. J. Hamers, "Photo-Illuminated Diamond as a Solid-State Source of Solvated Electrons in Water for Nitrogen Reduction," *Nature Materials* 12 (2013): 836–841.

45. L. Zhang and R. J. Hamers, "Photocatalytic Reduction of CO_2 to CO by Diamond Nanoparticles," *Diamond and Related Materials* 78 (2017): 24–30.

46. Z. Zhang, Y. Dai, and B. Huang, "The Electronic Properties and Electron Affinity of the Hydrogenated Nanodiamonds With Surface Reconstructions," *Applied Surface Science* 255 (2008): 2623–2626.

47. F. Buchner, T. Kirschbaum, A. Venerosy, et al., "Early Dynamics of the Emission of Solvated Electrons From Nanodiamonds in Water," *Nanoscale* 14 (2022): 17188–17195.

48. K. W. Wong, S. T. Lee, R. W. M. Kwok, Y. W. Lam, and H. Kawarada, "Electron Affinity and Surface Re-Ordering of Homoepitaxial Diamond (100)," *Japanese Journal of Applied Physics* 35 (1996): 5444.

49. R. Jones, J. E. Lowther, and J. Goss, "Limitations to n-Type Doping in Diamond: The Phosphorus-Vacancy Complex," *Applied Physics Letters* 69 (1996): 2489–2491.

50. D. Y. Liu, L. C. Hao, Y. Teng, et al., "Nitrogen Modulation of Boron Doping Behavior for Accessible *n*-Type Diamond," *APL Materials* 9 (2021): 081106.

51. T. Yoshikawa, H. Asakawa, T. Matsumoto, et al., "CO_2 Reduction by Visible-Light-Induced Photoemission From Heavily N-Doped Diamond Nano-Layer," *Carbon* 218 (2024): 118689.

52. J. Barkl, A. M. Zaniewski, F. Koeck, and R. J. Nemanich, "Diamond Photochemistry With Visible Light," *Diamond and Related Materials* 96 (2019): 195–197.

53. P. Bouvier, D. Delabouglise, A. Denoyelle, B. Marcus, M. Mermoux, and J.-P. Petit, "Photosensitization of Boron-Doped Diamond by Surface Grafting of Pyrene Groups," *Electrochemical and Solid-State Letters* 8 (2005): E57–E61.

54. W. S. Yeap, X. Liu, D. Bevk, et al., "Functionalization of Boron-Doped Nanocrystalline Diamond With N3 Dye Molecules," *ACS Applied Materials & Interfaces* 6 (2014): 10322–10329.

55. T. Hirose, Y. Maeno, and Y. Himeda, "Photocatalytic Carbon Dioxide Photoreduction by $Co(bpy)_3{}^{2+}$ Sensitized by $Ru(bpy)_3{}^{2+}$ Fixed to Cation Exchange Polymer," *Journal of Molecular Catalysis A: Chemical* 193 (2003): 27–32.

56. Y. Sano, A. Onoda, and T. Hayashi, "Photocatalytic Hydrogen Evolution by a Diiron Hydrogenase Model Based on a Peptide Fragment of Cytochrome c556 With An Attached Diiron Carbonyl Cluster and An Attached Ruthenium Photosensitizer," *Journal of Inorganic Biochemistry* 108 (2012): 159–162.

57. A. Krüger, F. Kataoka, M. Ozawa, et al., "Unusually Tight Aggregation in Detonation Nanodiamond: Identification and Disintegration," *Carbon* 43 (2005): 1722–1730.

58. S. H. Wadman, M. Lutz, D. M. Tooke, et al., "Consequences of N,C,N′- and C,N,N′-Coordination Modes on Electronic and Photophysical Properties of Cyclometalated Aryl Ruthenium(II) Complexes," *Inorganic Chemistry* 48 (2009): 1887–1900.

59. E. A. Medlycott and G. S. Hanan, "Designing Tridentate Ligands for Ruthenium(II) Complexes With Prolonged Room Temperature Luminescence Lifetimes," *Chemical Society Reviews* 34 (2005): 133–142.

60. F. Buchner, T. Kirschbaum; A. Venerosy, et al., "Early Dynamics of the Emission of Solvated Electrons From Nanodiamonds in Water," *Nanoscale* 14 (2021): 17188–17195.

61. A. Baron, C. Herrero, A. Quaranta, et al., "Click Chemistry on a Ruthenium Polypyridine Complex. An Efficient and Versatile Synthetic

Route for the Synthesis of Photoactive Modular Assemblies," *Inorganic Chemistry* 51 (2012): 5985–5987.

62. R. Graupner, J. Ristein, L. Ley, and C. Jung, "Surface-Sensitive K-Edge Absorption Spectroscopy on Clean and Hydrogen-Terminated Diamond (111) and (100) Surfaces," *Physical Review B* 60 (1999): 17023–17029.

63. J.-C. Arnault, "X-Ray Photoemission Spectroscopy Applied to Nanodiamonds: From Surface Chemistry to In Situ Reactivity," *Diamond and Related Materials* 84 (2018): 157–168.

64. M. Borgwardt, M. Wilke, I. Y. Kiyan, and E. F. Aziz, "Ultrafast Excited States Dynamics of $[Ru(bpy)_3]^{2+}$ Dissolved in Ionic Liquids," *Physical Chemistry Chemical Physics* 18 (2016): 28893–28900.

65. A. Chemin, I. Levine, M. Rusu, et al., "Surface-Mediated Charge Transfer of Photogenerated Carriers in Diamond," *Small Methods* 7 (2023): 2300423.

66. J. F. Morar, F. J. Himpsel, G. Hollinger, G. Hughes, and J. L. Jordan, "Observation of a C-1s Core Exciton in Diamond," *Physical Review Letters* 54 (1985): 1960–1963.

67. L. Weinhardt, O. Fuchs, D. Batchelor, et al., "Electron-Hole Correlation Effects in Core-Level Spectroscopy Probed by the Resonant Inelastic Soft X-Ray Scattering Map of C60," *The Journal of Chemical Physics* 135 (2011): 104705.

68. D. Miliaieva, A. S. Djoumessi, J. Cermak, et al., "Absolute Energy Levels in Nanodiamonds of Different Origins and Surface Chemistries," *Nanoscale Advances* 5 (2023): 4402–4414.

69. M. Borgwardt, M. Willke, I. Y. Kiyan, and E. F. Aziz, "Ultrafast Excited States Dynamics of $[Ru(bpy)_3]^{2+}$ Dissolved in Ionic Liquids," *Physical Chemistry Chemical Physics* 18 (2016): 28893–28900.

70. T. Petit, M. Pflüger, D. Tolksdorf, J. Xiao, and E. F. Aziz, "Valence Holes Observed in Nanodiamonds Dispersed in Water," *Nanoscale* 7 (2015): 2987–2991.

71. B. Wu, F. Amargianou, J.-D. Förster, et al., "Water Confinement in Nitrogen-Rich Nanoporous Carbon Materials Revealed by In Situ Scanning Transmission X-Ray Microscopy," *Advanced Functional Materials* 34 (2024): 2406528.

72. T. Petit, H. Yuzawa, M. Nagasaka, et al., "Probing Interfacial Water on Nanodiamonds in Colloidal Dispersion," *The Journal of Physical Chemistry Letters* 6 (2015): 2909–2912.

73. A. Cannizzo, F. van Mourik, W. Gawelda, G. Zgrablic, C. Bressler, and M. Chergui, "Broadband Femtosecond Fluorescence Spectroscopy of $[Ru(bpy)_3]^{2+}$," *Angewandte Chemie International Edition* 45 (2006): 3174–3176.

74. S. Wallin, J. Davidsson, J. Modin, and L. Hammarström, "Femtosecond Transient Absorption Anisotropy Study on $[Ru(bpy)_3]^{2+}$ and $[Ru(bpy)(py)_4]^{2+}$. Ultrafast Interligand Randomization of the MLCT State," *The Journal of Physical Chemistry A* 109 (2005): 4697–4704.

75. P. T. Cesana, B. X. Li, S. G. Shepard, et al., "A Biohybrid Strategy for Enabling Photoredox Catalysis With Low-Energy Light," *Chem* 8 (2022): 174–185.

76. J. A. Kloepfer, V. H. Vilchiz, V. A. Lenchenkov, A. C. Germaine, and S. E. Bradforth, "The Ejection Distribution of Solvated Electrons Generated by the One-Photon Photodetachment of Aqueous I− and Two-Photon Ionization of the Solvent," *The Journal of Chemical Physics* 113 (2000): 6288–6307.

77. A. Lübcke, F. Buchner, N. Heine, I. V. Hertel, and T. Schultz, "Time-Resolved Photoelectron Spectroscopy of Solvated Electrons in Aqueous NaI Solution," *Physical Chemistry Chemical Physics* 12 (2010): 14629–14634.

78. J. F. Brennecke and B. E. Gurkan, "Ionic Liquids for CO_2 Capture and Emission Reduction," *The Journal of Physical Chemistry Letters* 1 (2010): 3459–3464.

79. M. J. Muldoon, S. N. V. K. Aki, J. L. Anderson, J. K. Dixon, and J. F. Brennecke, "Improving Carbon Dioxide Solubility in Ionic Liquids," *The Journal of Physical Chemistry B* 111 (2007) 9001–9009.

80. X. Li, S. Li, J. Xu, et al., "Synergy of Nitrogen Vacancies and Nanodiamond Decoration in g-C_3N_4 for Boosting CO_2 Photoreduction," *Applied Surface Science* 600 (2022): 154199.

Supporting Information

Additional supporting information can be found online in the Supporting Information section.

Supporting File: adfm74390-sup-0001-SuppMat.pdf.